HAL
open science

GPS and GLONASS observations of large-scale traveling ionospheric disturbances during the 2015 St. Patrick's Day storm

Irina Zakharenkova, Elvira Astafyeva, Iurii Cherniak

To cite this version:

Irina Zakharenkova, Elvira Astafyeva, Iurii Cherniak. GPS and GLONASS observations of large-scale traveling ionospheric disturbances during the 2015 St. Patrick's Day storm. Journal of Geophysical Research Space Physics, 2016, 121 (12), pp.12,138-12,156. 10.1002/2016JA023332 . insu-02635317

HAL Id: insu-02635317

https://insu.hal.science/insu-02635317

Submitted on 29 May 2020

HAL is a multi-disciplinary open access archive for the deposit and dissemination of scientific research documents, whether they are published or not. The documents may come from teaching and research institutions in France or abroad, or from public or private research centers.

L'archive ouverte pluridisciplinaire **HAL**, est destinée au dépôt et à la diffusion de documents scientifiques de niveau recherche, publiés ou non, émanant des établissements d'enseignement et de recherche français ou étrangers, des laboratoires publics ou privés.

AGU PUBLICATIONS

JGR

Journal of Geophysical Research: Space Physics

RESEARCH ARTICLE

10.1002/2016JA023332

Special Section:
Geospace system responses to the St. Patrick's Day storms in 2013 and 2015

Key Points:
- Global view on LSTID development was derived from GPS and GLONASS data
- LSTIDs from opposite hemispheres converge over geomagnetic equator in South America
- "Super" LSTIDs with wavefront length of ~10000 km found in North America and Europe

Supporting Information:
- Supporting Information S1
- Figure S1
- Movie S1
- Movie S2

Correspondence to:
I. Zakharenkova,
zakharen@ipgp.fr

Citation:
Zakharenkova, I., E. Astafyeva, and I. Cherniak (2016), GPS and GLONASS observations of large-scale traveling ionospheric disturbances during the 2015 St. Patrick's Day storm, *J. Geophys. Res. Space Physics*, *121*, 12,138–12,156, doi:10.1002/2016JA023332.

Received 15 AUG 2016
Accepted 18 NOV 2016
Accepted article online 20 NOV 2016
Published online 22 DEC 2016

©2016. American Geophysical Union. All Rights Reserved.

GPS and GLONASS observations of large-scale traveling ionospheric disturbances during the 2015 St. Patrick's Day storm

Irina Zakharenkova[1], Elvira Astafyeva[1], and Iurii Cherniak[2]

[1]Institut de Physique du Globe de Paris, Paris Sorbonne Cité, Université Paris Diderot, Paris, France, [2]Space Radio Research Center, University of Warmia and Mazury, Olsztyn, Poland

Abstract Using a comprehensive database of ~5300 ground-based Global Navigation Satellite Systems (GNSS) stations we have investigated large-scale traveling ionospheric disturbances (LSTIDs) during 17–18 March 2015 (St. Patrick's Day storm). For the first time, the high-resolution, two-dimensional maps of the total electron content perturbation were made using not only GPS but also GLONASS measurements. Several LSTIDs originated from the auroral regions in the Northern and Southern Hemispheres were observed simultaneously over Europe, North America, and South America. This storm is considered as a two-step main phase storm. During the first main phase LSTIDs propagated over the whole daytime European region and over high latitudes of North America. During the second main phase we report (1) intense LSTIDs propagated equatorward in North America and Europe, (2) convergence of several LSTIDs originated from the opposite hemispheres in the interference zone over geomagnetic equator in South America, and (3) "super" LSTIDs with the wavefront length of more than 10,000 km observed simultaneously in North America and Europe. LSTIDs observed in three sectors had wavelength of ~1200–2500 km and wave periods of ~50–80 min. During the recovery phase on the background of the negative ionospheric storm developed over North America we detect signatures of the stream-like structures elongated within the latitudinal range of 29°N–42°N across the U.S. These structures persisted through the nighttime to the early morning from 04 UT to 13 UT on 18 March 2015, and they were associated with the subauroral polarization stream-induced nighttime ionospheric flows.

1. Introduction

Travelling ionospheric disturbances (TIDs) have been intensively studied for many decades [*Munro*, 1948; *Hines*, 1960; *Chan and Villard*, 1962; *Georges*, 1968; *Davis and Da Rosa*, 1969; *Davis*, 1971; *Francis*, 1974; *Hunsucker*, 1982; *Hocke and Schlegel*, 1996; *Kirchengast*, 1997; *Afraimovich et al.*, 2000]. TIDs are generally considered as ionospheric signatures of atmospheric gravity waves (AGWs) in the thermosphere [*Hines*, 1960]. According to *Georges* [1968] and *Hunsucker* [1982] TIDs can be divided into two classes: medium-scale TIDs (MSTIDs) and large-scale TIDs (LSTIDs). MSTIDs have horizontal wavelengths of several hundred kilometers, horizontal velocities of 100–250 m/s, and periods of 15–60 min, whereas LSTIDs have a horizontal scale of more than 1000 km, horizontal speeds of 400–1000 m/s, and periods of 30–180 min. Occurrence of LSTIDs is generally related to geomagnetic activity, and they travel from the polar regions toward the equator, while MSTIDs are typically observed at midlatitudes during both quiet and disturbed conditions.

TIDs were observed by a variety of techniques, such as ionosondes [e.g., *Bowman*, 1965; *Maeda and Handa*, 1980; *Tedd and Morgan*, 1985], incoherent scatter radars [e.g., *Natorf et al.*, 1992; *Kirchengast et al.*, 1996; *Nicolls and Heinselman*, 2007; *van De Kamp et al.*, 2014], satellite beacons [e.g., *Evans et al.*, 1983], HF Doppler radars [e.g., *Georges*, 1968], and airglow imaging [e.g., *Mendillo et al.*, 1997; *Shiokawa et al.*, 2003, 2005; *Duly et al.*, 2013]. Since mid-1990s, ground-based segment of the Global Positioning System (GPS) started to grow up extensively from several hundred stations worldwide to more than 6000 stations today. It provides a new opportunity to study TID structure and evolution by using high-resolution, two-dimensional maps of the ionospheric total electron content (TEC). *Saito et al.* [1998] were the first to show two-dimensional maps of TEC perturbations caused by MSTIDs over Japan using a very dense network consisting of about 1000 GPS receivers. Further, MSTID and LSTID characteristics were investigated using dense GPS receiver networks in Japan [e.g., *Saito et al.*, 2001; *Shiokawa et al.*, 2002; *Tsugawa et al.*, 2003; *Tsugawa and Saito*, 2004; *Nishioka et al.*, 2009; *Hayashi et al.*, 2010], North America [e.g., *Nicolls et al.*, 2004; *Tsugawa et al.*, 2007; *Kotake et al.*, 2007;

Onishi et al., 2009], and less dense GPS networks in Europe [*Borries et al*., 2009; *Jakowski et al*., 2012; *Otsuka et al*., 2013] and China [*Song et al*., 2013; *Ding et al*., 2014]. Apart from that, *Ding et al*. [2014] reported results of the comparative study of LSTIDs using GPS networks in North America and China. Several papers reported GPS observation of auroral LSTIDs simultaneously over North and South America during geomagnetic storms of 29–30 October 2003 [*Valladares et al*., 2009] and of 26 September 2011 [*Pradipta et al*., 2016]. It is important to note that all these studies were done using only GPS measurements. In the present paper, for the first time, we include measurements of the Russian GNSS - GLONASS (In Russian: GLObalnaya NAvigazionnaya Sputnikovaya Sistema), in order to considerably increase a number of available observations and to obtain better spatiotemporal resolution of the resulted TEC perturbation maps. Then, by using the collected data from ~5300 ground-based GNSS stations we investigate LSTIDs over three regions—Europe, North America, and South America—during the 2015 St. Patrick's Day storm.

2. Data and Method Used

In this paper we focused on three geographical regions: North America, South America, and Europe. We process and analyze GPS and GLONASS raw measurements provided by a number of regional and global networks of GNSS receivers: the International GNSS Service, the University NAVSTAR Consortium, the Continuously Operating Reference System (CORS), the Scripps Orbit and Permanent Array Center, the EUREF Permanent GNSS network, the Federal Agency for Cartography and Geodesy in Germany, Institut Geographique National in France, the Finnish Reference Network (FGI-FinnRef), the NOANET GNSS Network in Greece, the Natural Resources Canada's Canadian Geodetic Survey, the Canadian High Arctic Ionospheric Network, Red Geodesica Nacional Activa (Instituto Nacional de Estadística y Geografía) in Mexico, the Brazilian Network for Continuous Monitoring (RBMC), and the Red Argentina de Monitoreo Satelital Continuo (RAMSAC CORS). In addition, data from more than 330 GNSS stations were provided by the Swedish geodetic network (SWEPOS). Overall we processed data from ~5300 GNSS receivers. We considerably increase number of available observation by processing signals not only U.S. GPS but also Russian GNSS system—GLONASS. The advantage of GLONASS, as compared to GPS, is that GLONASS has an orbit inclination of ~65° that is 10° higher than the GPS orbit inclination [see *Hofmann-Wellenhof et al*., 2008; *ICD GLONASS*, 2008; *Jeffrey*, 2015]. This feature is important for high-latitude regions, where a multisystem GNSS receiver can track the GLONASS navigation signals for much longer time and with higher-elevation angles than the GPS ones; for middle and equatorial latitudes a modern multisystem GNSS receiver provides 6-8 additional links to the GLONASS satellites per epoch that can increase a number of derived observations by a factor of 1.5–2 comparing to GPS only. Figure 1a shows the distribution of the permanent GNSS receivers, color depict ability of receiver to track GPS satellites only or both system GPS and GLONASS. It is clearly seen that the territory of the U.S. has the best coverage by ground-based stations, while multisystem GNSS receivers are mainly located in the European region, eastern part of the U.S., and in Brazil. The vast territory of Canada has rather sparse distribution of the GNSS stations.

To calculate the TEC from the frequency-differenced GPS measurements we use the well-known algorithms [*Blewitt*, 1990; *Hofmann-Wellenhof*, 2001]. From the differential carrier phase (L_1 and L_2) and pseudorange (P_1 and P_2) measurements we derive the slant TEC (sTEC), defined as the line integral of the electron density from a GNSS satellite to a ground-based receiver:

$$sTEC_L = \left(\frac{L_1}{f_1^2} - \frac{L_2}{f_2^2}\right) \cdot \frac{f_1^2 \cdot f_2^2}{f_1^2 - f_2^2} \cdot \frac{c}{K} \tag{1}$$

$$sTEC_P = (P_2 - P_1) \cdot \frac{f_1^2 \cdot f_2^2}{f_1^2 - f_2^2} \cdot \frac{1}{K} \tag{2}$$

where $f_1 = 1575.42$ MHz and $f_2 = 1227.60$ MHz are the carrier frequencies of the GPS signals, L_1 and L_2 are the corresponding phase paths of radio signals at f_1 and f_2, $K = 40.3$ m^3/s^2, and $c = 3 \times 10^8$ m/s is the speed of light in vacuum.

For the GLONASS measurements, the particular feature is the following. Unlike the GPS system, where each satellite transmits radio signals at two fixed carrier frequencies f_1 and f_2, the present GLONASS uses a

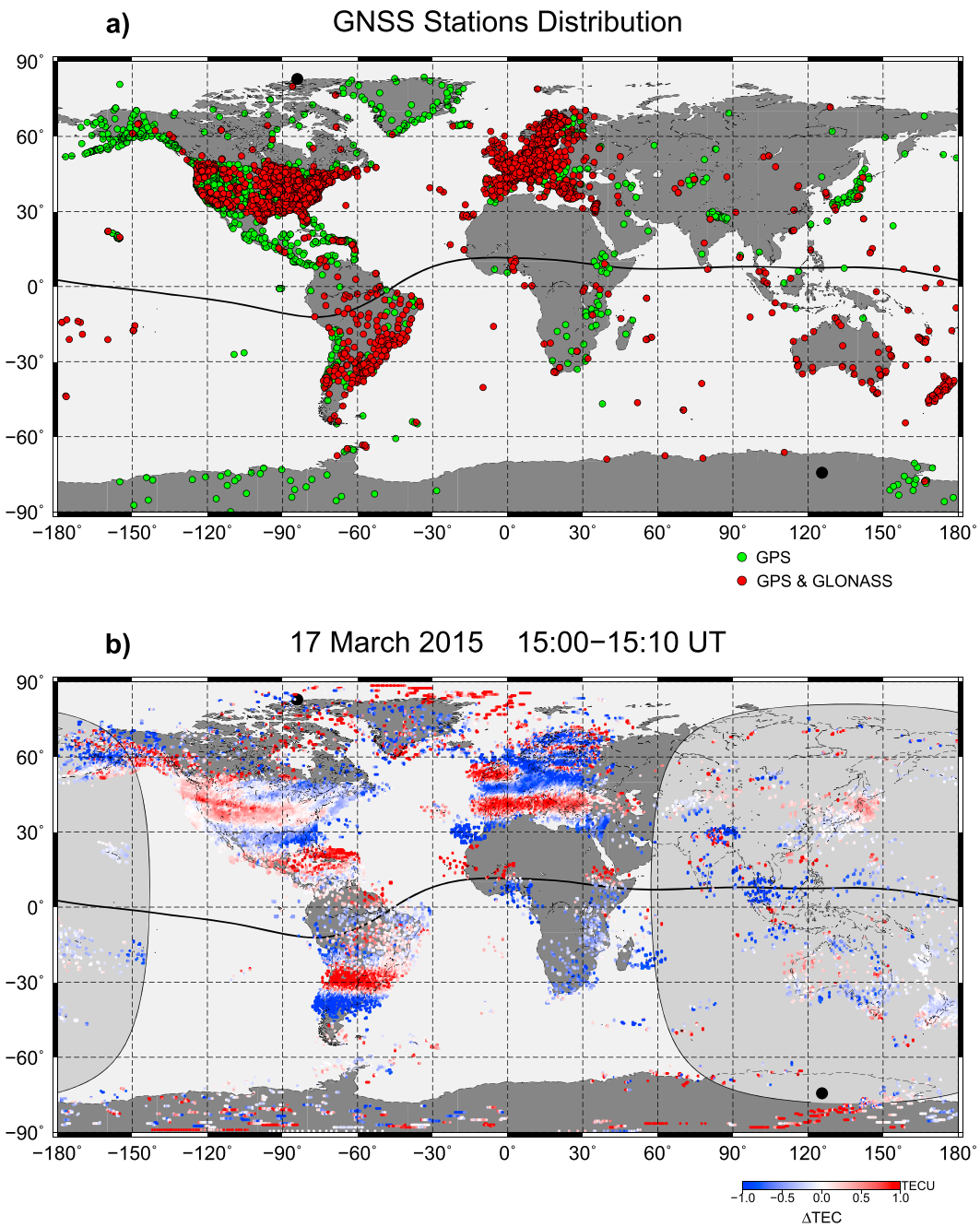

Figure 1. (a) Geographical distribution of the ground-based GNSS stations provided measurements of navigational signals for GPS only (green dots) and for both systems GPS and GLONASS (red dots). (b) Sample of global two-dimensional map of TEC perturbation for 15:00–15:10 UT on 17 March 2015.

frequency division multiple access technique to distinguish the signals coming from different satellites and all GLONASS satellites transmit the same code at different frequencies [*ICD-GLONASS*, 2008]. These frequencies are defined through frequency numbers k by

$$f_1 = (1602.0 + 0.5625 \cdot k)\ [\text{MHz}] \tag{3}$$

$$f_2 = (1246.0 + 0.4375 \cdot k)\ [\text{MHz}] \tag{4}$$

where k is the frequency channel number ($k = -7, -6, -5, \ldots, 0, \ldots, 6$). GLONASS accomplishes system operation (24 satellites and only 15 channels) by having antipodal satellites transmit on the same frequency.

Antipodal satellites are in the same orbit plane separated by 180 in argument of latitude [*Jeffrey*, 2015]. This is possible because the paired satellites will never appear at the same time in view of an operational ground-based receiver. The frequency channel numbers for GLONASS satellites can be found in an actual GLONASS almanac [e.g., *Russian IAC PNT*, 2016]. The sTEC is further calculated by using the same formulas (1) and (2) as in the case of GPS measurements.

It should be noted that we use a single station approach, which means that raw measurements from each station are processed separately from other stations. Moreover, GPS and GLONASS raw measurements even for a single station are also processed independently in parallel by different routines. This approach allows us to avoid possible issues related to accuracy of single set of differential code biases (DCBs) determined from the multistations processing with further correction of the TEC solution on station-by-station basis; also, it minimizes well-known issues related to GLONASS interfrequency biases, which can vary significantly for the same GLONASS satellite across different GPS/GLONASS receiver brands [e.g., *Wanninger*, 2012].

The carrier phase measurements can be affected by cycle slips, which are sudden changes in the integer phase ambiguity due to the phase tracking loop within the receiver. The cycle slip may be as small as one or a few cycles or contain millions of cycles. Here we use two approaches for cycle slip detection—the wide-lane Melbourne-Wübbena linear combination [*Melbourne*, 1985; *Wübbena*, 1985] and method of differencing geometry-free phase observations (*sTEC_L*) with estimation of rate of TEC changes similar to that of *Horvath and Crozier* [2007].

To remove carrier phase ambiguity, we use a phase-leveling code algorithm described by *Ma and Maruyama* [2003], where baseline B_{rs} is computed as the average difference between pseudorange-derived *sTEC_P* and phase-derived *sTEC_L* values along continuous arc of satellite-receiver measurements:

$$sTEC = sTEC_L + B_{rs} \tag{5}$$

$$B_{rs} = \frac{\sum (sTEC_P - sTEC_L)\cdot \sin^2\alpha}{\sum \sin^2\alpha} \tag{6}$$

where the square sine of the satellite's elevation α is included as a weighting factor, as the pseudorange with low-elevation angle is apt to be affected by the multipath effect and the reliability decreases. For the ground-based GNSS data we select the elevation angle cutoff as 30° to avoid the multipath effect.

The resulting slant TEC should be calibrated from instrumental biases due to differential equipment path delays in the GPS/GLONASS satellites and ground-based receiver. To convert slant TEC into vertical TEC (hereafter TEC) we used a single-layer model, where the ionosphere is approximated by a spherical thin shell at 350 km altitude.

$$\mathrm{vTEC} = \mathrm{sTEC}\times\cos\chi - b_s - b_r \tag{7}$$

$$\chi = \arcsin\left(\frac{R_E\cos\alpha}{R_E + h}\right) \tag{8}$$

where χ is the zenith angle, α is the elevation angle, R_E is the mean radius of the Earth, h is the height of the ionospheric layer (here $h = 350$ km), and b_s and b_r are the satellite and receiver biases (DCBs).

Unknown satellites and receiver differential code biases are obtained during solution of overdetermined system of polynomial expansion equations with use of the least squares fitting technique and singular value decomposition. As a result for each station we obtain TEC values along all visible (GPS or GLONASS) satellites with 30 s sampling period. TEC values are presented in TEC units, 1 TECU = 10^{16} el/m^2. Here we applied a single-layer model with a fixed altitude of the layer at 350 km to all geographical latitudes, but we can also mention several other approaches which can be applied to retrieve vertical TEC at equatorial latitudes, particularly, using the higher-elevation cutoff mask [e.g., *Paul et al.*, 2011; *Sur et al.*, 2015] or using the modified dip latitude [e.g., *Azpilicueta et al.*, 2006; *Brunini and Azpilicueta*, 2010].

Further, to derive the TID-related perturbation component in the TEC data we use a method similar to that of *Tsugawa et al.* [2007]. The perturbation components of TEC were obtained by detrending TEC with 1 h running mean (over ±30 min centered on the corresponding time) for all GNSS stations and visible satellites. Then, the two-dimensional maps of the detrended TEC were constructed by binning all available GPS and GLONASS TEC data to 0.5° × 0.5° cells in geographic latitude and longitude. Temporal resolution of the

constructed maps was 10 min. Here to create two-dimensional maps we do not use any spatial interpolation or horizontal smoothing procedure. Using two-dimensional maps of the TEC perturbation component we derive the propagation characteristics of the storm-induced LSTID. We define LSTID as the TEC perturbations that satisfy the following criteria in the same way as *Ding et al*. [2014] in consistence with the LSTID definition by *Hunsucker* [1982]: (1) the TEC perturbation has amplitude exceeding 0.5 TECU, (2) the horizontal wavelength of the TEC perturbations is longer than 1000 km, and (3) the TEC perturbation has more than two phase fronts and propagates on the map. To estimate the LSTID propagation characteristics we used the same technique as described by *Kotake et al*. [2007]. It includes determination of the LSTID propagation direction, which is assumed to be perpendicular to the wavefront of the TEC perturbations. To estimate horizontal wavelength and period of LSTIDs, we construct a slice of the TEC perturbation component as a function of time and geographical location along a line parallel to the LSTID propagation direction. The horizontal wavelength of LSTID is defined as twice the distance between the minimum and maximum of the TEC perturbations. The period of the LSTID is twice average of the time lag between the negative and positive phase fronts, whereas amplitude is estimated as an average deviation of the TEC perturbations in peaks from the zero level. The horizontal phase velocity (v) of the LSTID is obtained from $v = \lambda/T$, where λ is the horizontal wavelength and T is the period of the LSTID. We should emphasize that due to integral nature of the TEC measurements this technique of the TID detection in two-dimensional TEC maps does not provide information about the TID's vertical wavelength. Only incoherent scatter radar (ISR) measurements allow to estimate the TID's vertical scale and amplitude in the whole thickness of the ionosphere, even above the F_2 layer peak. Joint analysis of the two-dimensional TEC maps and ISR data, like it was demonstrated by *Nicolls et al*. [2004] with the Arecibo ISR and by *van De Kamp et al*. [2014] with the EISCAT (European Incoherent Scatter) ISR, can give information on both vertical and horizontal structures of the TIDs. In the present paper we focused on the horizontal characteristics of the TID's propagation.

3. Geomagnetic Disturbances of 17–18 March 2015

The space weather conditions during the 2015 St. Patrick's Day storm were described in detail in several recent papers [e.g., *Kamide and Kusano*, 2015; *Astafyeva et al*., 2015; *Cherniak et al*., 2015; *Zhang et al*., 2015]. The sudden storm commencement was registered at ~04:45 UT, and then there was a quick drop of the *SYM-H* index to the value of −226 nT, observed at ~23:00 UT, with a couple of local minima of −93 and −164 nT at ~09:40 and ~17:40 UT, respectively (see variations of the interplanetary magnetic field (IMF) and geomagnetic parameters in Figure S1 in the supporting information). After the shock arrival, the northward IMF B_z component reached the value of ~25 nT. At ~05:30 UT the IMF B_z turned southward and reached the first minimum value of −18 nT at 06:15 UT. Then the IMF B_z sharply turned northward and varied drastically between north and south over ~8 h. After ~13:40 UT the B_z turned southward again and remained southward directed until the end of this day. The *SYM-H* index reached two local minima of −93 and −150 nT at 09:40 and 16:30 UT, respectively. The minimum of the *SYM-H* index of −226 nT occurred at 23 UT. The auroral activity index *AE* depicts two intensification peaks at ~09 UT and ~14 UT. Between these two peaks a northward turning of B_z was observed. The midlatitude magnetic activity index *Kp* reached the value of 8.

4. Results and Discussion

4.1. Overall View on the LSTIDs Observed in GPS and GLONASS Data

We analyzed GPS and GLONASS observations derived from numerous regional and global networks of the ground-based GNSS segment in order to investigate main characteristics and spatial-temporal evolution of the LSTIDs during the 2015 St. Patrick's Day storm. Figure 1b shows a sample of a global map of the TEC perturbation component constructed for the time interval of 15:00–15:10 UT on 17 March 2015. This map clearly indicates an occurrence of several LSTIDs with positive and negative phase fronts in the European and American sectors. We note that Europe and North and South America have better data coverage as compared to other regions. Unfortunately, the Chinese network CMONOC (Crustal Movement Observation Network of China) does not provide GNSS data in a standard open access mode, whereas dense networks in Japan, Australia, and New Zealand are able to cover rather limited spatial areas and were not analyzed here. That is why, in this paper we focused on observations of several LSTIDs over three different geographical regions: Europe and North and South America.

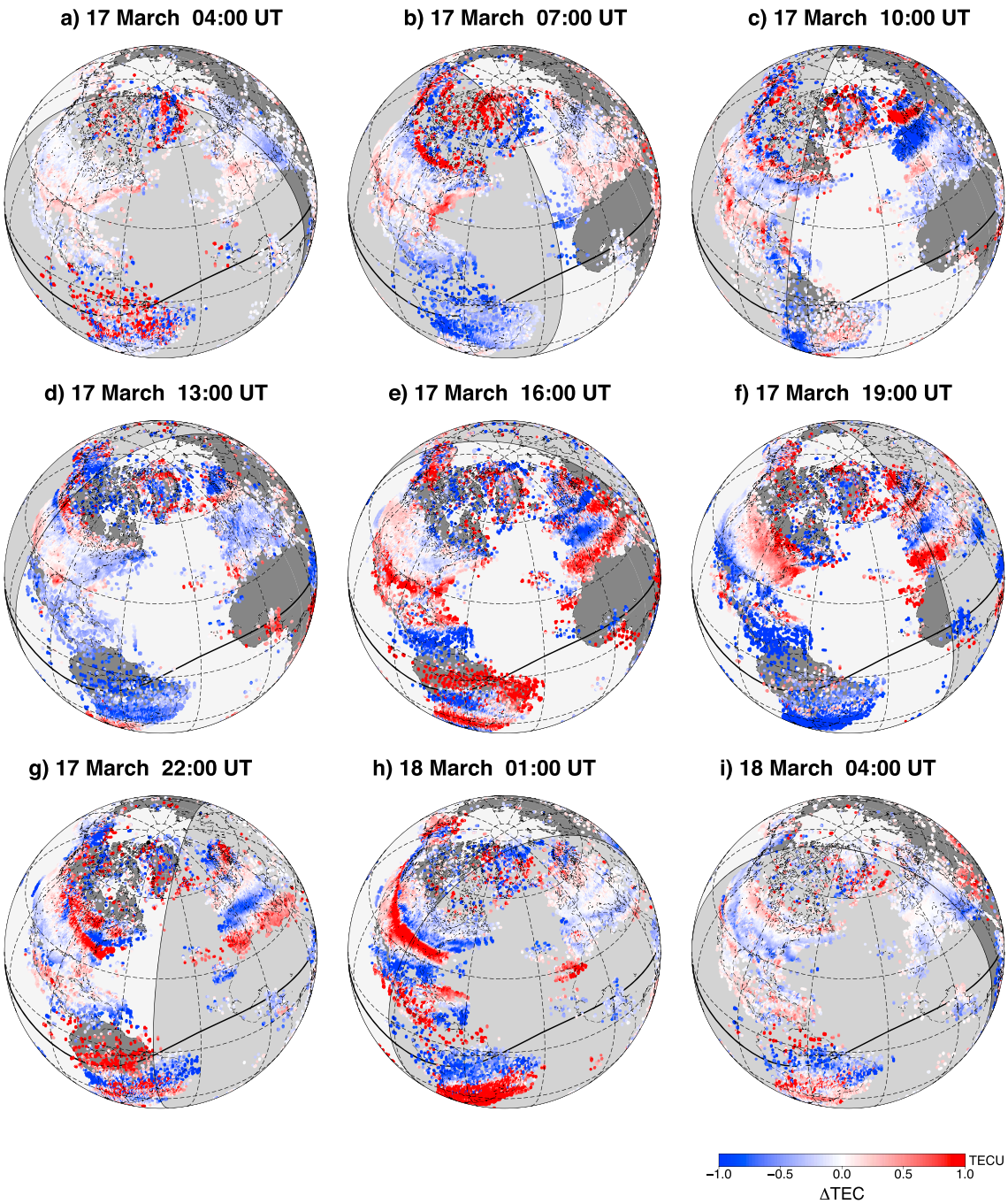

Figure 2. Global view on two-dimensional maps of TEC perturbations with focus on the American and European sectors for different instants of time (a–i) on 17–18 March 2015. The large-scale trend was subtracted with a 60 min running average. The grey shaded area shows the nighttime period regarding the terminator position calculated at 100 km altitude. The geomagnetic equator is shown by the black solid line, and black dots show the position of the magnetic poles. Full set of the two-dimensional maps with 10 min time interval is available in Movies S2 and S3 in the supporting information.

Figure 2 presents a sequence of the two-dimensional maps of TEC perturbations constructed with focus on the American and European sectors with 10 min time interval for different instants of time (every 3 h) on 17–18 March 2015. The grey shadow area superimposed on each map depicts nighttime zone with the terminator line calculated at 100 km altitude. Movies S2 and S3 in the supporting information demonstrate the full series of these maps with 10 min time resolution for 17 and 18 March 2015, respectively. The presented results (Figure 2 and Movies S2 and S3) show the storm-induced dynamics of LSTIDs

during main and recovery phases (first day) of the storm. Figure 2a illustrates the prestorm conditions where (1) TIDs generated by the sunrise terminator can be clearly recognized over the European region and (2) weak MSTID structures are observed at middle latitudes of North America and Europe.

Generation of the TIDs by the moving sunrise terminator is an important and interesting feature related to the AGWs [e.g., *Afraimovich*, 2008; *Forbes et al*., 2008], which could be effectively recognized in such two-dimensional maps of TEC perturbation [e.g., *Song et al*., 2013]. During 03:30–06:00 UT we observe the sunrise terminator passage over Europe and equatorial latitudes of Africa; the terminator-induced TIDs have a wavefront aligned the terminator and have latitudinal range of more than 15°. These TIDs were clearly observed over South America during 08–10 UT (e.g., Figure 2c), whereas the terminator passage across North America during 10:30–13:30 UT have generated the TIDs with less prominent signatures due to interference with the storm-induced LSTIDs.

First effects of the increased geomagnetic activity were found over high-latitude regions of the Northern Hemisphere after ~06 UT on 17 March 2015 (see Movie S2). Figures 2b–2h demonstrate the snapshots of global overview of LSTID propagation at different moments of the geomagnetic storm. In particular, Figure 2e shows the dayside hemisphere with several LSTIDs propagated equatorward in Europe and North America and even reached geomagnetic equator in South America at 16:00 UT.

Further, we analyze meridional "slices" at three considered regions in order to compare evolution of the storm-induced LSTIDs with time during the main storm phase on 17 March 2015. Meridional slices are constructed as an average of the TEC perturbations within the band of $\pm 5°$ around a selected geographical longitude and plotted as a function of geographic latitude and time in the similar way as in *Nicolls et al*. [2004]. Figure 3 shows the TEC perturbations as a function of geographic latitude and time constructed along the most representative geographical longitudes: 10°E in Europe, 85°W in North America, and 65°W in South America during the whole day of 17 March 2015. Right vertical axis at Figures 3b–3d presents the corresponding corrected geomagnetic latitudes. The slopes of the most intense TEC perturbation (marked by dashed black lines) directly indicate that the propagation velocity speed of the LSTIDs crossed the considered longitude.

Figure 3 (top) presents the variation of the auroral electrojet (*AE*) index on 17 March 2015. The *AE* index characterizes the magnetospheric energy deposed to the auroral oval, and it is usually used as a proxy of Joule heating. As reviewed by *Hunsucker* [1982], two possible causes of LSTIDs, i.e., the Lorentz force and the Joule heating, can be considered in the auroral zone. Joule heating can produce traveling atmospheric disturbances, which interact with the ionosphere and produce LSTIDs with long horizontal wavelengths propagated equatorward.

For the prestorm period during 00–04 UT on 17 March 2015 the variation of the TEC perturbed component along three meridional slices did not reveal signatures of LSTIDs. In the European sector at ~05 UT one can note a negative disturbance (marked by black dashed line) associated with the sunrise terminator passage. The first peak in *AE* index of ~772 nT was registered at ~06:38 UT. Shortly after that, the meridional slice over North America revealed an appearance of the first signatures associated with the TID generation at high latitudes. This TID (marked by black dashed line near 07 UT in Figure 3c) propagated over the nighttime North America region and reached geographic latitude of ~47°N. LSTIDs with smaller amplitude were propagated over already sunlitted European sector, but for a longer distance and at ~08:30 UT they reached geographic latitude of ~40°N. After 07 UT the *AE* index indicates an intensification of the auroral activity during the first main phase of the storm, which lasted till ~11–12 UT; during this period the *AE* index had a peak of ~1016 nT at 08:52 UT. During this phase LSTIDs with larger amplitude were generated and propagated equatorward. The LSTID that propagated over North America (marked by black dashed line near 08–09 UT in Figure 3c) had rather short duration of lifetimes and propagated not so far in comparison with ones in the European sector. During the first main phase the LSTIDs were predominantly propagated in the daytime sector in the European region and two LSTID events were registered during 09–10 UT and 10–12 UT. These waves with an amplitude larger than 1 TECU propagated equatorward from the polar region of Europe with an estimated horizontal velocity of ~600–700 m/s.

After 12 UT the second main phase of the storm started and a new intensification of auroral activity with the *AE* index above 2000 nT was registered during 13–15 UT, as well as further peaks of *AE* during the rest of the day. These peaks in *AE* correlate well with an occurrence of LSTIDs observed in North America and Europe. During this time LSTIDs over North America propagated further equatorward than latitude of ~40°N as

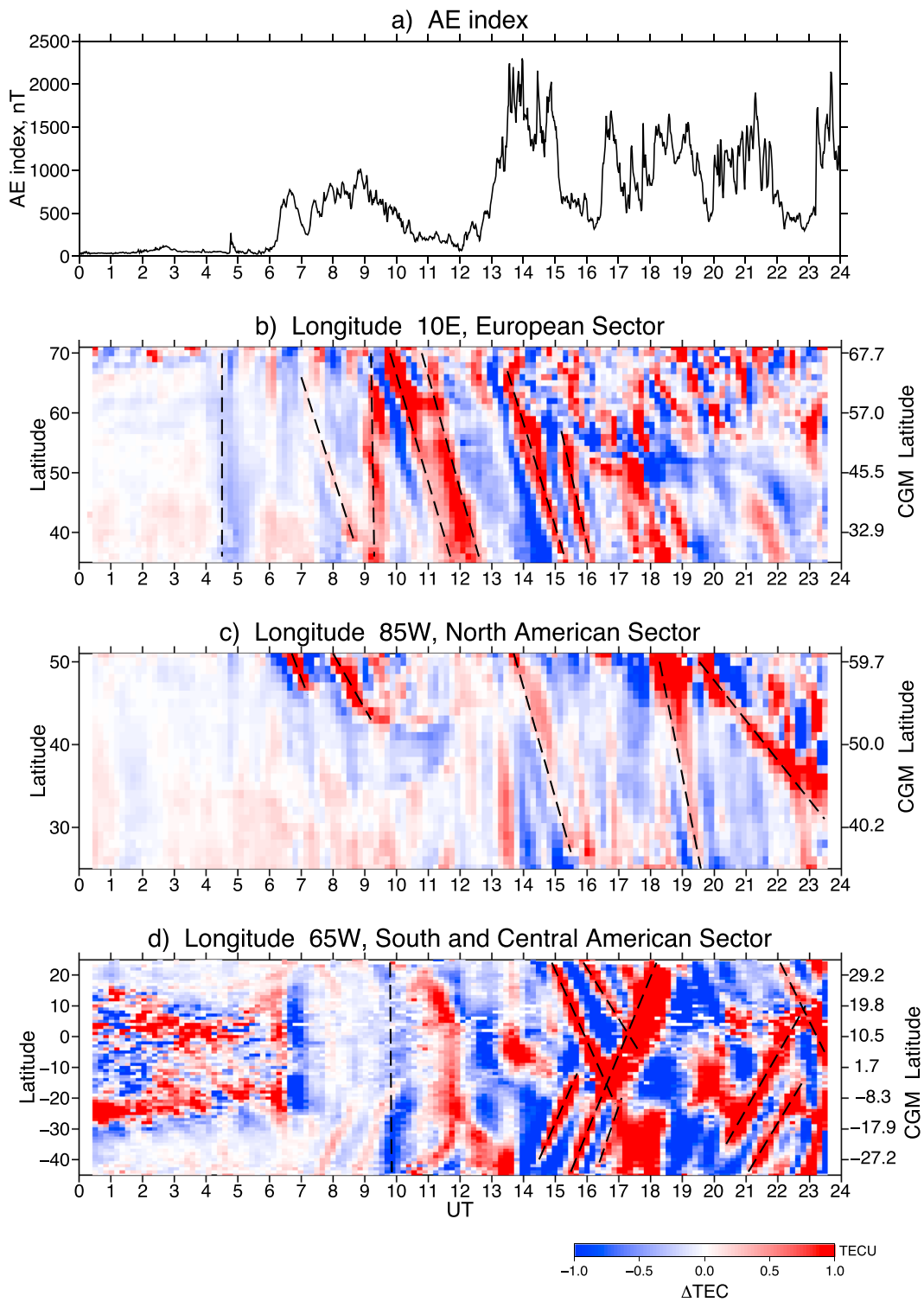

Figure 3. Comparison of (a) the auroral electrojet (*AE*) index and TEC perturbations as a function of geographic latitude and time, evaluated along (b) 10°E in Europe, (c) 85°W in North America, and (d) 65°W in South America during 00–24 UT of 17 March 2015. The left vertical axis at Figures 3b–3d graphs shows the geographic latitudes and the right axis—corresponding latitudes in corrected geomagnetic (CGM) coordinates.

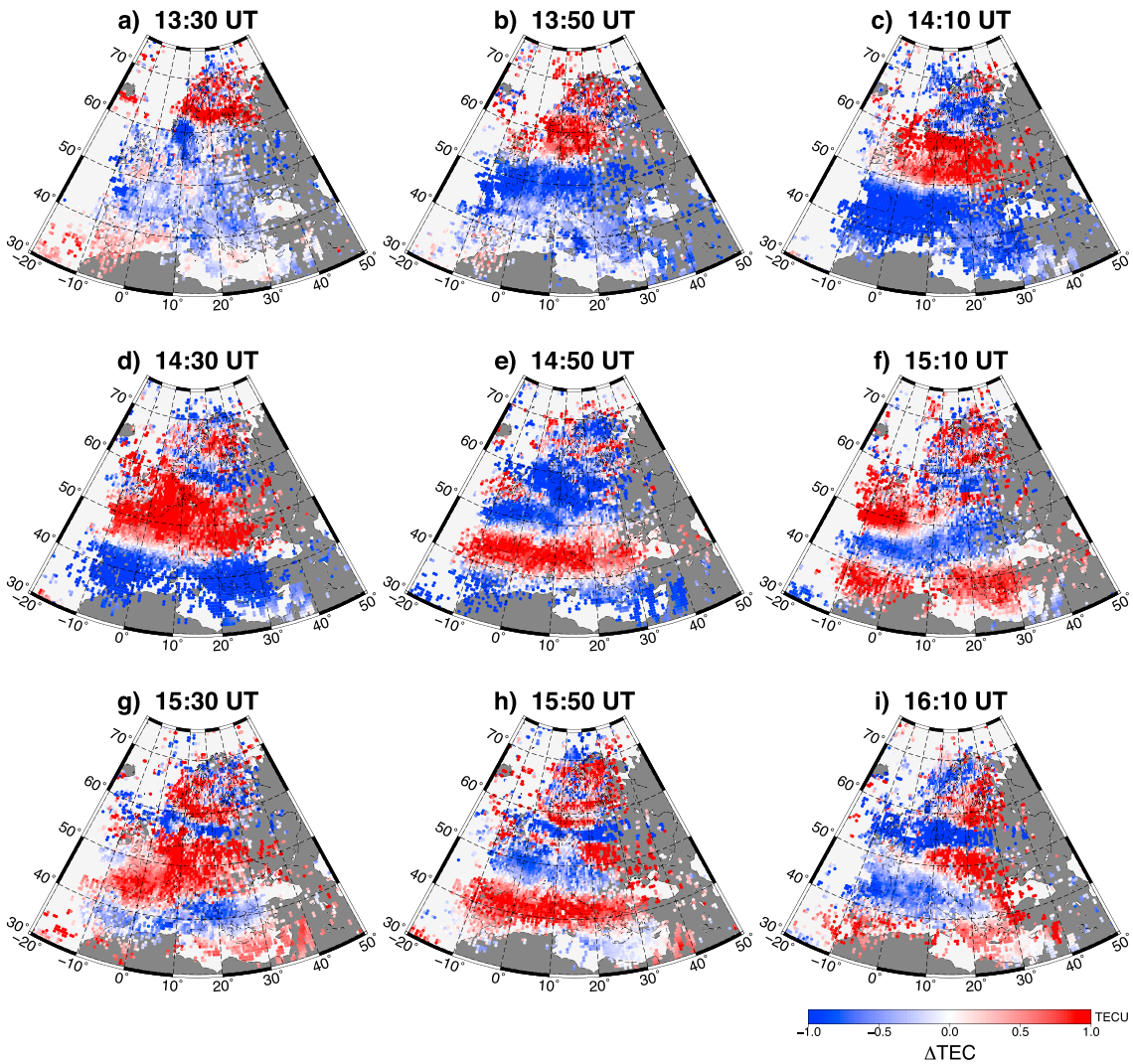

Figure 4. Two-dimensional maps of TEC perturbations over Europe for different instants of time (a–i) during 14:40–16:50 UT on 17 March 2015.

compared with the first main phase; this period corresponds also to the daytime conditions in this geographical sector, while sunrise terminator crossed 90°W at ~12 UT (Figure 3c). We can distinguish two separated events with LSTIDs propagated over North America at 18–19 UT and 20–23 UT. The meridional slice for South and Central American sector (Figure 3d) depicts TID generated by the sunrise terminator passage at ~10 UT and occurrence of several LSTIDs with southward and northward slopes, indicating an equatorward propagation from opposite hemispheres. During the second main phase at 15–17 UT several LSTIDs reached equatorial latitudes and converged in the interference zone over the geomagnetic equator.

In the next sections we consider the LSTID characteristics over three geographical regions in more detail.

4.2. Daytime Sector in Europe

The European region can be characterized by a well-developed GNSS network with proper data coverage in north-south direction (30°N–70°N). This network consists of the large number of small national or regional networks; the majority of stations provides both GPS and GLONASS measurements.

Figure 4 presents the series of the two-dimensional regional maps of TEC disturbances observed over Europe during the second main phase of the storm. Each map covered the range of geographic latitudes of 30°N–70°N and longitudinal range of 20°W–50°E. These maps were constructed with 10 min resolution and presented here with 20 min interval for 13:30 UT–16:10 UT on 17 March 2015. Figures 4a–4f

demonstrate the evolution of the LSTIDs in space propagated across Europe. Figure 4a depicts an appearance of LSTID with an amplitude of ~1.1 TECU over Sweden and Norway at ~13:30 UT. This LSTID propagated equatorward with horizontal velocity of ~500–650 m/s, and at 15:10 UT it reached the southern borders of Europe and went away from the zone covered by GNSS stations. At the same time, the other two LSTIDs entered into the European region. The first LSTID appeared over the Great Britain (50°N–60°N, 10°W–0°W), and its main part of the wavefront seems to be located westward in the Atlantic Ocean (Figures 4e and 4f). LSTIDs observed over Europe had wave amplitude of ~1–1.3 TECU, wave period of ~50 min, and wavelength of ~1600–1900 km. The second LSTID appeared in the north of Sweden and Norway. Both LSTIDs propagated equatorward over Europe with increased amplitude and spatial scale. This increase of LSTID amplitude could be explained by that of the background TEC, which is generally larger at low latitudes than at high latitudes. If the AGWs propagate with a constant amplitude, the total amount of plasma variation caused by the AGWs could be larger at lower latitudes, resulting in the latitudinal variation of the LSTID amplitude [e.g., *Tsugawa et al*., 2007].

4.3. Daytime Sector in South America

Recent deployment of the dense regional GNSS networks in Brazil (RBMC) and Argentina (RAMSAC CORS) significantly increases the GNSS data coverage over South America, while the most northern part of this continent has still rather sparse distribution of GNSS stations. Despite the limitations caused by the sparse data distribution in the north, it allows us to investigate in detail the spatial evolution of LSTIDs generated in the Southern Hemisphere.

We observe an interesting phenomenon with convergence of several LSTIDs propagated equatorward over North and South America in the vicinity of the geomagnetic equator. Figure 5 presents a set of the TEC perturbation maps over South America at 14:40–16:50 UT on 17 March 2015. On the first map (Figure 5a) we can observe an appearance of the first LSTID (#1) generated in the Southern Hemisphere and propagated equatorward over South America within the latitudinal range of 35°S–40°S. Twenty minutes later (Figure 5b) LSTID #1 moves further toward the equator, whereas new LSTID #2 comes from North America to the Caribbean region. The LSTID #2 had wave amplitude of ~1.5 TECU and wavelength of ~2500 km. Next maps (Figures 5c–5f) illustrate further equatorward propagation of both LSTIDs. The estimated propagation velocities were ~600–700 m/s and ~600 m/s for LSTIDs #1 and #2, respectively. The two LSTIDs start to converge at 15:50–16:00 UT in the vicinity of the geomagnetic equator within the latitudinal range of 0°S–10°S (Figures 5f and 5g). So LSTID #2 that originated from the North America auroral region crossed the geographic equator and entered to the Southern Hemisphere after 16:00 UT, where it met LSTIDs that originated in the Southern Hemisphere.

During convergence of LSTID #1 and #2 near the geomagnetic equator the third disturbance (#3) appeared from south of the considered region and also propagated equatorward (Figures 5d–5h). Further, at 16:20–16:30 UT the LSTID #3 reached the equatorial region where previous LSTIDs #1 and #2 had already stopped their movement. Movement of LSTIDS with the opposite direction leads to their interference close to the geomagnetic equator and further formation of a positive TEC disturbance just over this zone. Figures 5j and 5k demonstrate that incoming LSTID #3 also entered the interference zone near geomagnetic equator, while new LSTIDs #4 and #5 appeared from north and south directions. The LSTIDs observed over South America had wave amplitude of ~0.9–1.2 TECU, wave period of ~60 min, and wavelength of ~2500 km. This event was observed after the most significant increase of the *AE* index during the whole storm, *AE* index rose to more than 2000 nT at 13–15 UT, which indicates an increase of Joule heating in auroral region of both hemispheres and further generation of LSTIDs with large amplitudes.

We should note that only a few papers reported GPS-based observations of auroral LSTID propagation simultaneously over North and South America during geomagnetic storms, namely, for events of 29–30 October 2003 [*Valladares et al*., 2009] and 26 September 2011 [*Pradipta et al*., 2016]. *Pradipta et al*. [2016] found that LSTIDs propagated from opposite hemispheres with speed of ~700 m/s interfered near the geomagnetic equator over South America and even continued their propagation into the opposite hemisphere. It is important to note that these previous studies were based on GPS measurements only, as well as lesser number of GNSS stations over South America in 2003 and 2011. In the given paper, we used an increased number of GNSS stations together with GLONASS measurements that allow us to recognize signatures of LSTID appearance, their interhemispheric propagation, and their interference in the vicinity of the geomagnetic equator (geographic latitudes of 0°S–10°S).

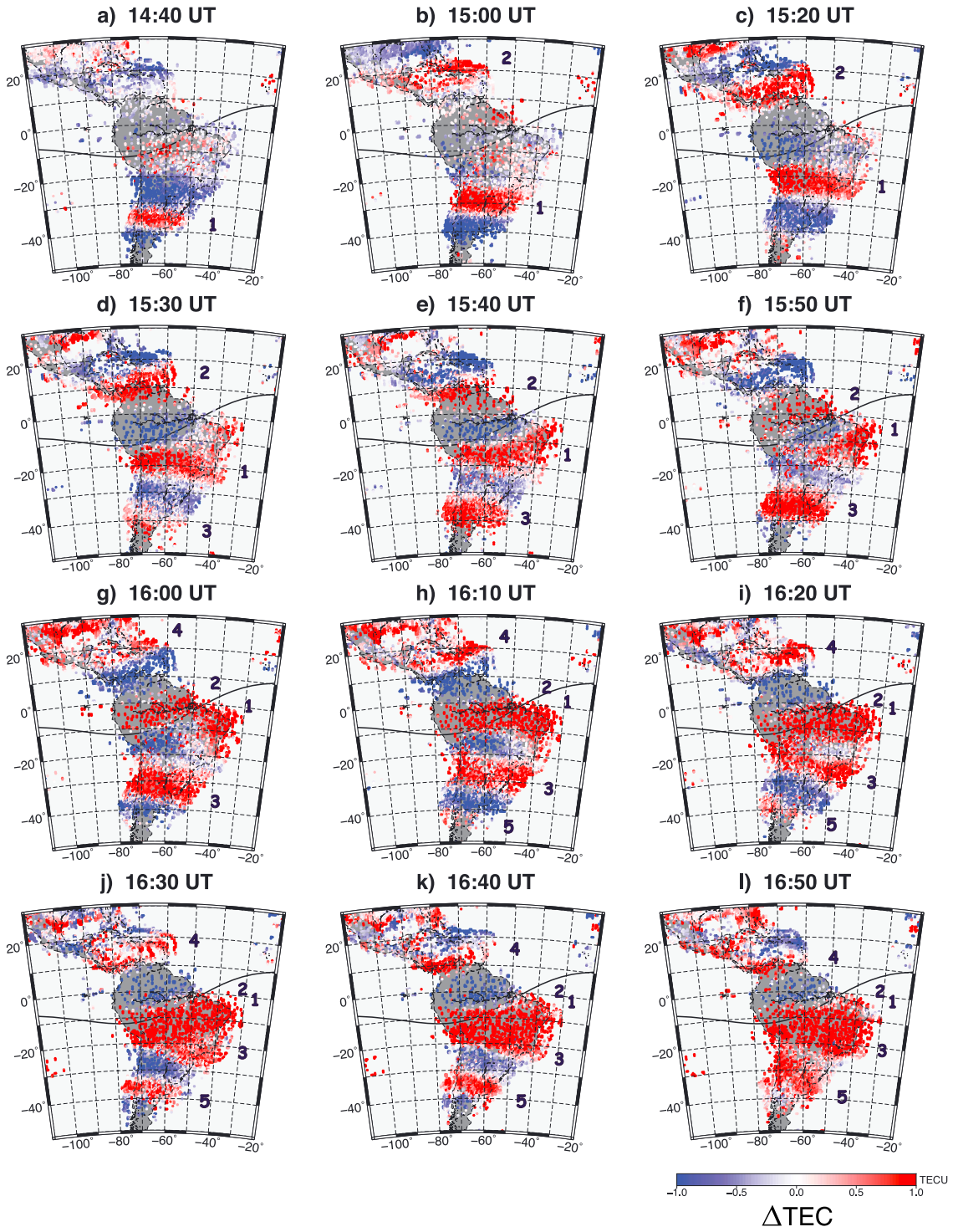

Figure 5. Two-dimensional maps of TEC perturbations over South America for different instants of time (a–i) during 14:40–16:50 UT on 17 March 2015. The top row shows the 10 min maps with 20 min interval. The numbers indicate the LSTIDs that propagated equatorward from North and South America. The geomagnetic equator is shown by the black solid line.

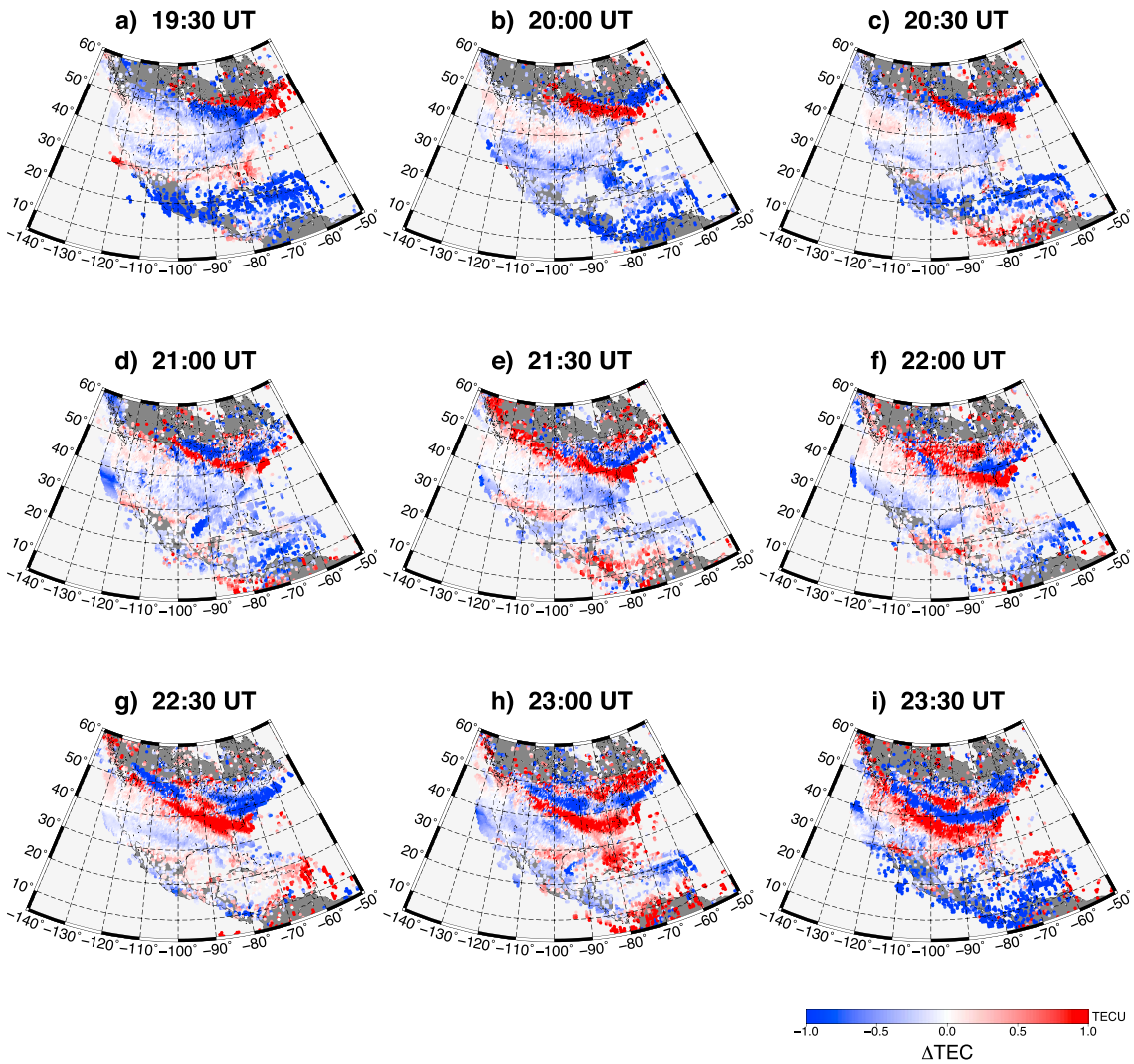

Figure 6. Two-dimensional maps with LSTID propagation over North America for different instants of time (a–i) during 19:30–23:30 UT on 17 March 2015.

4.4. Daytime Sector in North America

As shown in Figure 3c, the intense LSTIDs that propagated equatorward across North America below latitudes of 40°N (50°N geomagnetic latitude) were observed after 13 UT, namely, after the onset of the second main phase and during daytime condition in North America. Trains of LSTIDs that originated in auroral region of the Northern Hemisphere propagated across North America and even reached the geomagnetic equator in South America during 14–16 UT as it was discussed in section 4.3. Two separated events with LSTIDs that propagated over North America were registered at 18–19 UT and 20–23 UT (Figure 3c).

Figure 6 presents the set of two-dimensional maps of TEC perturbations constructed with 10 min resolution and demonstrated here with 30 min interval during 19:30 UT–23:30 UT on 17 March 2015. Each map covered range of geographic latitudes of 5°N–60°N and longitudinal range of 140°W–50°W, which include a wide area from Canada to the Caribbean region. Figure 6a depicts an LSTID structure that appeared in the form of narrow arc over Eastern Canada at 19:30 UT. During next hour this structure propagated equatorward with the estimated velocities of ~350–400 m/s. This LSTID had wave amplitude of ~0.8–1.0 TECU, wave period of ~50 min, and wavelength of ~1000–1200 km. After 21:30 UT the second structure appeared from north over this region. Further both LSTIDs with an amplitude of disturbance above 1 TECU propagate slowly across North America. The shape of the wavefront at this time was mainly controlled by the Earth geomagnetic field, and it looked like an arc extended from Western Canada to Florida.

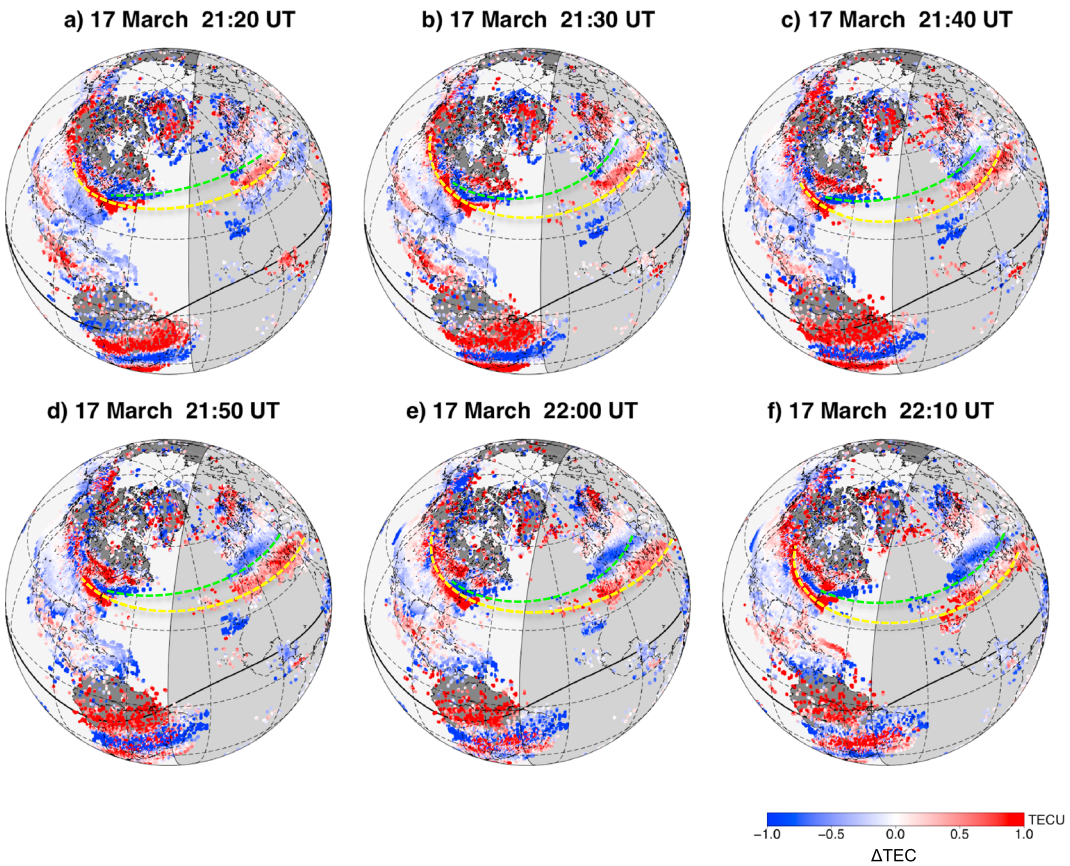

Figure 7. Global two-dimensional maps of TEC perturbations with 10 min interval during 21:20 UT–22:10 UT on 17 March 2015. The yellow and green dashed lines indicate the locations of positive and negative wavefronts of the super LSTID that propagated simultaneously over North America and Europe. The grey shaded area shows the nighttime period regarding the terminator position at 100 km altitude.

We should note that this time interval of 21–23 UT corresponds to the maximal development of the geomagnetic storm (the minimal excursion of the *SYM-H* index) and next period of the auroral activity intensification. Thus, generation of the intense LSTIDs should be expected during this period. We considered this time in more detail. Figure 7 demonstrates the set of global two-dimensional maps of TEC perturbations with 10 min interval during 21:20 UT–22:10 UT on 17 March 2015. Here we find that these LSTIDs observed over North America are in fact only segment of much larger structure, extended through the Atlantic Ocean and Europe. We called this structure as "super" LSTIDs. The yellow and green dashed lines in Figure 7 indicate the location of positive and negative wavefronts of the super LSTID. We note that these wavefronts propagated simultaneously over North America and Europe with similar signatures observed at the GNSS stations in the Atlantic Ocean. The super LSTID wavefront length was more than 10,000–12,000 km. In such a way, rather slow velocities of LSTID propagation over North America can be explained by the fact that the rest part of the super LSTID wavefront propagated over Atlantic Ocean and Europe with much higher speed. Besides, the slower propagating LSTID over North America could be related to the "curling" of the wavefront toward the west and the local afternoon. This effect was previously reported by *Afraimovich et al*. [2000] for the 25 September 1998 geomagnetic storm. Earlier, LSTIDs in the form of solitary wave with an annular front were found to be generated at the equatorward edge of the auroral oval and traveled equatorward in the Northern Hemisphere to 20°N–25°N latitudes almost without changing of its annular front shape during superstorm of 29–30 October 2003 [*Afraimovich and Voeykov*, 2004; *Perevalova et al*., 2008]. In the present case, we observe part of such super LSTID with much larger, probably annular wavefront. We should also note that in order to estimate spatial characteristics of LSTIDs, particularly with large or annular wavefront, the spatial distribution of the ground-based instruments should be essentially larger than LSTID's sizes—it becomes feasible only after an extensive deployment of the ground-based GNSS networks during the last decade.

Further studies of an LSTID occurrence using global GNSS data can provide a clue to an understanding of the dynamical response of the ionosphere/thermosphere system to severe geomagnetic storms, particularly dependencies of LSTID amplitude, wavefront length, and propagation characteristics on different causing mechanisms at high latitudes, such as Joule heating, Lorentz forces, and particle precipitation.

4.5. Nighttime Sector in North America

Another interesting phenomenon apparent in the two-dimensional TIDs maps over North America is the stream-like structures observed during the storm recovery phase on 18 March 2015. During this time rather low values of electron density and TEC were observed over middle and high latitudes of North America due to development of the negative ionospheric storm in this region [e.g., *Astafyeva et al.*, 2015].

Figure 8 presents the set of two-dimensional maps of TEC perturbations constructed with 10 min resolution and demonstrated here with 30 min interval during 04:30 UT–13:00 UT on 18 March 2015. All two-dimensional TID maps clearly demonstrate presence of the fine structures elongated across the whole U.S. from 25°N, 75°W to 42°N, 130°W. We found these disturbances to be persisted within the same spatial band during all nighttime hours. During the considered time the amplitudes of the observed disturbances slightly varied within the range of 0.25–0.45 TECU, which corresponds mostly to the MSTID amplitude. It is important to note that these stream-like structures did not exhibit any equatorward or southwestward (like nighttime MSTIDs) propagation. Interestingly, the passage of the sunrise terminator at 11:00–11:30 UT seems to diminish or eliminate an appearance of these disturbances (Figures 8n and 8o). However, next maps for 12:00–13:00 UT reveal persistence of these disturbances at the background of the terminator-induced TIDs.

One of the possible mechanisms that can contribute into formation of these persistent TEC structures at mid-latitudes is the subauroral polarization stream (SAPS) electric fields [*Foster and Burke*, 2002; *Foster et al.*, 2007] and SAPS-related processes. SAPS flows overlap the plasmasphere edge and coincident with midlatitude ionospheric trough [*Foster and Vo*, 2002]; they provide a significant convective force moving plasma against corotation from the dusk sector toward the noontime cusp forming so-called storm-enhanced density (SED) plume [*Foster*, 1993]. Passage of the SED plume was observed in the high-resolution TEC maps over North America during 16–23 UT on 17 March 2015 [*Liu et al.*, 2015; *Cherniak et al.*, 2015]. This SED event occurred in the premidnight sector during the storm main phase. SED cannot be formed during nighttime conditions on 18 March 2015 due to plasma density decrease at the source region at midlatitudes, but SAPS flows can still remain. Earlier, *Basu et al.* [2008] reported a new class of GPS TEC fluctuations—storm-induced nighttime ionospheric flows at midlatitudes, which are seen during geomagnetic storms in the absence of large-scale SED and associated gradients, but in the presence of intense SAPS channels within the main ionospheric trough. In particular, they discussed plasma instability mechanism which operates between the SAPS-driven density trough and the increased density at the equatorward edge of the trough, where opposing density and temperature gradients can generate plasma density irregularities.

Recently, *Zhang et al.* [2015] reported a significant poleward surge in thermospheric winds at subauroral and midlatitudes following the 17–18 March 2015 storm. These disturbances were observed over three sites within geographic latitudes 35°N–42°N and longitudes of 71°W–88°W in the American sector by Fabry-Perot interferometers (FPIs) at 630 nm wavelength. Prior to the wind disturbances, SAPS were measured by the Millstone Hill incoherent scatter radar between 20 and 02 UT. A strong westward ion drift, identified as SAPS, drove neutral particles westward, causing a strong westward neutral wind (~300 m/s) observed by multiple FPIs between 35 and 42°N latitudes in the American sector. Later, a poleward neutral wind response occurred at 02–04 UT on 18 March 2015 due to Coriolis force effects on the westward neutral wind. The poleward wind, directly observed by the FPIs, eventually reached 100 m/s amplitude in a few hours following the onset of SAPS. According to Figure 2 in *Zhang et al.* [2015] two FPIs UAO (40.13°N, 88.20°W) and PAR (35.2°N, 82.85°W) had registered a westward neutral wind till 07–08 UT on 18 March 2015. These observations are in a rather good temporal agreement with fine structures appeared in the corresponded latitudinal sector of the two-dimensional TID maps (Figure 8).

Further, we analyze one case with an occurrence of the nighttime stream-like structures in more detail involving other types of ionospheric measurements. Figures 9a and 9b present the two-dimensional maps of the TEC perturbation component and absolute TEC values, respectively, constructed for the moment 4:30–4:40 UT on 18 March 2015. TEC map depicts the deep ionospheric trough over midlatitudes of North America and increased density at low and equatorial latitudes. Here we were able to involve in situ

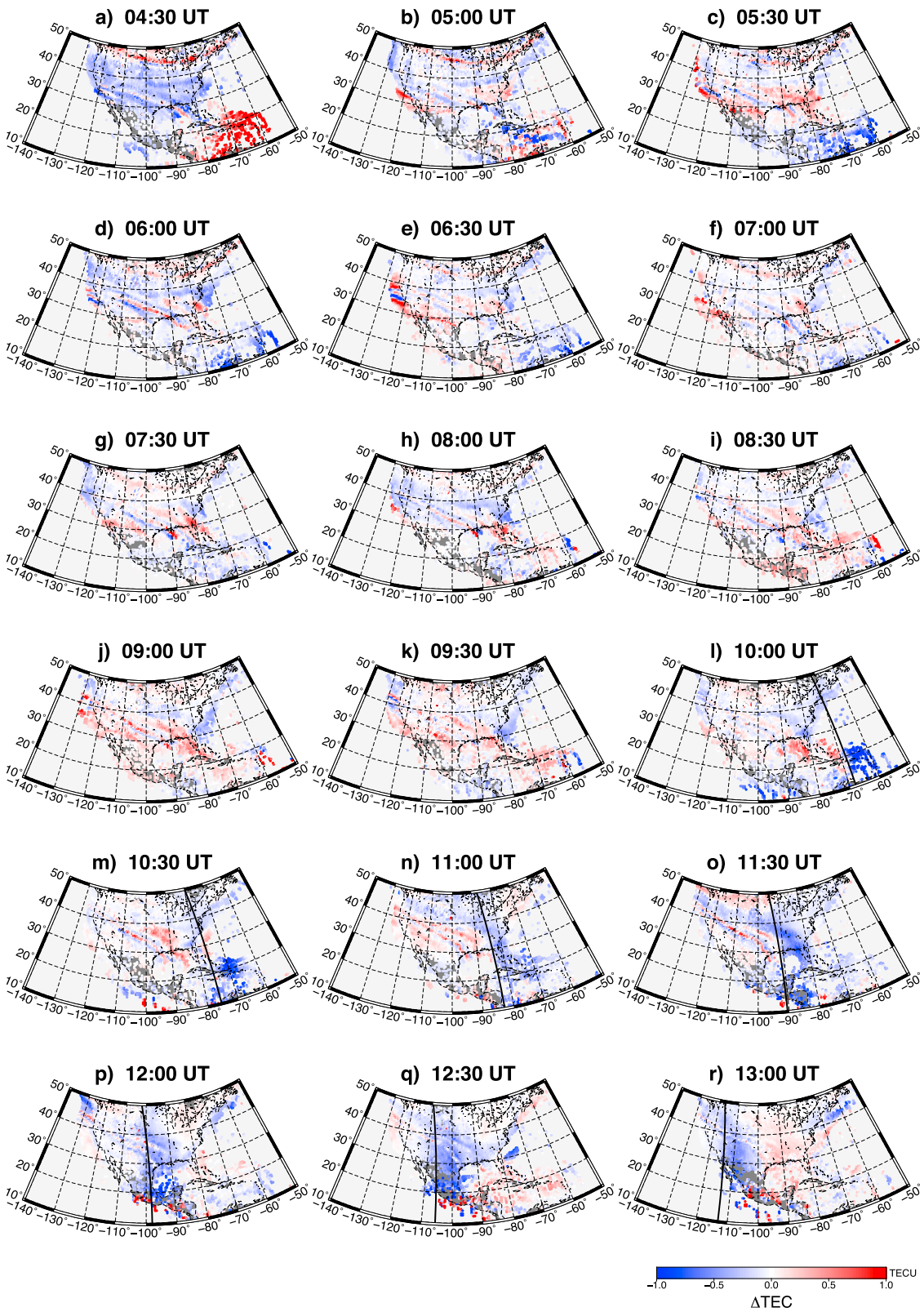

Figure 8. Two-dimensional maps of nighttime TEC perturbations observed over North America for different instants of time (a–r) during 4:30–13:00 UT on 18 March 2015. The black solid line superimposed on maps (Figures 8l–8r) depicts the position of the sunrise terminator at 100 km altitude.

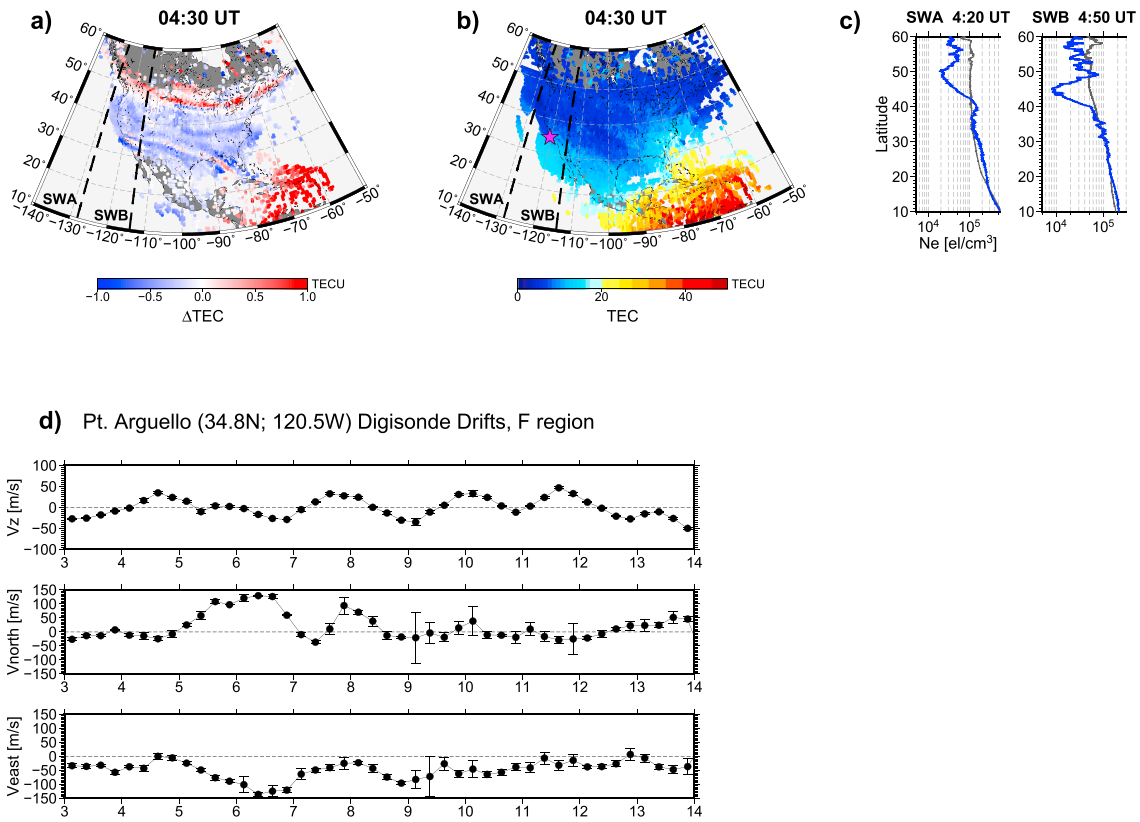

Figure 9. Two-dimensional maps of (a) TEC perturbation and (b) absolute vertical TEC constructed for the moment 4:30–4:40 UT on 18 March 2015 with superimposed Swarm A and B passes (dashed lines), (c) in situ electron density along Swarm A and B passes for 18 March (blue lines) and 16 March (grey lines), and (d) Point Arguello digisonde *F* region drifts during 03–14 UT on 18 March 2015. The magenta asterisk indicates the location of the Point Arguello digisonde.

electron density (N_e) measurements on board Swarm A and B satellites, which crossed the western part of the U.S. at ~4:20 UT and ~4:50 UT, respectively. In March 2015, the orbit altitude of the Swarm A and B satellites was ~465 km and ~515 km, respectively. Figure 9c shows the latitudinal profiles of in situ electron density along Swarm passes for 18 March (blue lines) and 16 March (grey lines). Both profiles demonstrate that the main ionospheric trough was observed at midlatitudes; its equatorward edge was at ~45°N geomagnetic latitude. The peak density inside the deep plasma trough was about 1 order of magnitude lower than that of quiet time conditions. We can see that the 1 Hz measurements of in situ plasma density on board Swarm registered noticeable fluctuations of the density within latitudinal range of 30°N–40°N, equatorward of the main trough. These fluctuations were more intense along the Swarm B satellite and coincided geographically with location of the stream-like structures on the TEC perturbation map (Figure 9a). Thus, these results are in consistence with the discussed by *Basu et al.* [2008] storm-induced nighttime ionospheric flows, which are observed at midlatitudes, below the equatorward edge of the main ionospheric trough.

As we mentioned above a strong westward ion drift, associated with SAPS, was registered by Millstone Hill ISR at the eastern coast of the U.S. and by several FPIs at the Central U.S. midlatitudes. In order to confirm the presence of westward drifts at the Pacific Ocean coast we analyze the plasma drifts of the ionospheric *F* layer derived from the Point Arguello (34.8°N, 120.5°W) digisonde measurements provided by the Global Ionospheric Radio Observatory [*Reinisch and Galkin*, 2011]. This digisonde (marked by asterisk on Figure 9 b) located at the western coast of the U.S., in the given case two Swarm overpasses, was in the direct vicinity from this station. The Digisonde Portable Sounders operate essentially as radar systems; i.e., they measure radar distances and angles of arrival of the received echoes. The observed echoes on the skymap are used to derive zenith and azimuth of the ionospheric tilt, as well as vertical and horizontal components of the bulk ionospheric motion across the sounder location. The drift velocity components are calculated from the line of site velocities (Doppler frequency shifts) of the skymap source points [*Reinisch et al.*, 1998]. The *F* layer drift

measurements over the Point Arguello digisonde during 03–14 UT on 18 March demonstrate that poleward wind (V_{north}) reached 100–150 m/s during 05–07 UT with another peak of ~50–80 m/s at 08 UT. The westward zonal drift (panel V_{east} in Figure 9d) was observed during practically the whole considered time. The westward drift was ~50 m/s with peaks of ~150 m/s during 06–07 UT and ~100 m/s at 09 UT; these values for Point Arguello station were even larger than those observed by the FPIs in the central part of the U.S. It should be noted that during the considered period of time, the vertical component (V_z) of plasma motion changed from negative to positive several times. Overall, the digisonde plasma drifts reveal that ionospheric plasma over this sounder drifted predominantly in westward or northwestward direction in the nighttime sector on 18 March 2015. From multiinstrument and multipoint observations we conclude on favorable conditions for development of the storm-induced nighttime ionospheric flows at midlatitudes, whose signatures were recognized as stream-like structures in the two-dimensional maps of the TEC perturbations over the North America region.

5. Conclusions

We analyzed GPS and GLONASS observations derived from ~5300 ground-based GNSS stations in order to investigate main characteristics and spatial-temporal evolution of the LSTIDs during the 2015 St. Patrick's Day storm. In this paper we present LSTID observations simultaneously over three different geographic regions: Europe and North and South America. In fact, they are the three most informative regions when they are considered together, because (1) they have dense networks of GNSS receivers, (2) their GNSS data cover a wide latitudinal extent between high latitudes of the Northern and Southern Hemispheres, and (3) their GNSS data cover a wide longitudinal extent between 130°W and 40°E in the Northern Hemisphere. Thus, simultaneous analysis of these three regions can provide new information about LSTID propagation on a global scale.

The obtained results can be summarized as follows:

1. The TIDs generated by moving sunrise terminator are clearly recognized in the two-dimensional maps of the TEC perturbations effective for LSTID detection.
2. During the first main phase of the storm LSTIDs propagated over the whole daytime European region and over high latitudes of North America.
3. During the second main phase we found (1) intense LSTIDs propagated equatorward in North America and Europe, (2) convergence of several LSTIDs originated from opposite hemispheres in the interference zone over geomagnetic equator in South America, and (3) super LSTIDs with wavefront length of more than 10,000 km observed simultaneously in North America and Europe.
4. During the recovery phase at the background of the negative ionospheric storm developed over North America we detect signatures of the stream-like structures elongated within the latitudinal range of 29°N–42°N across the U.S. These structures were persisted during the nighttime to the early morning from 04 UT to 13 UT on 18 March 2015, and they were associated with the SAPS-induced nighttime ionospheric flows.

Acknowledgments
This work is supported by the European Research Council under the European Union's Seventh Framework Program/ERC grant 307998. We acknowledge the use of the raw GNSS data provided by IGS (ftp://cddis.gsfc.nasa.gov), UNAVCO (ftp://data-out.unavco.org), CORS (ftp://geodesy.noaa.gov), SOPAC (ftp://garner.ucsd.edu), EPN (ftp://olggps.oeaw.ac.at), BKGE (ftp://igs.bkg.bund.de/euref/obs), IGN (ftp://rgpdata.ign.fr), SWEPOS (swepos.lantmateriet.se), FGI-FinnRef (euref-fin.fgi.fi), NOANET (www.gein.noa.gr), Natural Resources Canada (webapp.geod.nrcan.gc.ca), CHAIN (ftp://chain.physics.unb.ca/gps/), INEGI (ftp://geodesia.inegi.org.mx), RBMC (ftp://geoftp.ibge.gov.br/RBMC/), and RAMSAC CORS of National Geographic Institute of Argentina (www.igm.gov.ar/NuestrasActividades/Geodesia/Ramsac/). This paper uses ionospheric data from the USAF NEXION Digisonde network; the Nexion Program Manager is Mark Leahy. We thank B.W. Reinisch, UML, for making these ionograms available through the GIRO DriftExplorer tool (http://spase.info/VWO/DisplayData/GIRO/SKYMAP.PT15M). We acknowledge ESA for SWARM data (http://earth.esa.int/swarm) and use of NASA/GSFC's Space Physics Data Facility's OMNIWeb service for the data of the interplanetary and geophysical parameters. This is IPGP contribution 3808.

References

Afraimovich, E. L. (2008), First GPS-TEC evidence for the wave structure excited by the solar terminator, *Earth Planets Space*, *60*, 895–900, doi:10.1186/BF03352843.

Afraimovich, E. L., E. A. Kosogorov, L. A. Leonovich, K. S. Palamartchouk, N. P. Perevalova, and O. M. Pirog (2000), Determining parameters of large-scale traveling ionospheric disturbances of auroral origin using GPS-arrays, *J. Atmos. Solar Terrestrial Phys.*, *62*, 553–565, doi:10.1016/S1364-6826(00)00011-0.

Afraimovich, E. L., and S. V. Voeykov (2004), Experimental evidence of the existence of a solitary internal gravity wave in the Earth's atmosphere during a strong magnetic storm, *Dokl. Earth Sci.*, *399A*(9), 1301–1304.

Astafyeva, E., I. Zakharenkova, and M. Förster (2015), Ionospheric response to the 2015 St. Patrick's Day storm: A global multi-instrumentl overview, *J. Geophys. Res. Space Physics*, *120*, 9023–9037, doi:10.1002/2015JA021629.

Azpilicueta, F., C. Brunini, and S. M. Radicella (2006), Global ionospheric maps from GPS observations using modip latitude, *Adv. Sp. Res.*, *38*, 2324–2331, doi:10.1016/j.asr.2005.07.069.

Basu, S., S. Basu, J. J. Makela, E. Mackenzie, P. Doherty, J. W. Wright, F. Rich, M. J. Keskinen, R. E. Sheehan, and A. J. Coster (2008), Large magnetic storm-induced nighttime ionospheric flows at midlatitudes and their impacts on GPS-based navigation systems, *J. Geophys. Res.*, *113*, A00A06, doi:10.1029/2008JA013076.

Blewitt, G. (1990), An automatic editing algorithm for GPS data, *Geophys. Res. Lett.*, *17*, 199–202, doi:10.1029/GL017i003p00199.

Borries, C., N. Jakowski, and V. Wilken (2009), Storm induced large scale TIDs observed in GPS derived TEC, *Ann. Geophys.*, *27*, 1605–1612, doi:10.5194/angeo-27-1605-2009.

Bowman, G. G. (1965), Travelling disturbances associated with ionospheric storms, *J. Atmos. Terr. Phys.*, *27*, 1247–1261, doi:10.1016/0021-9169(65)90085-1.

Brunini, C., and F. Azpilicueta (2010), GPS slant total electron content accuracy using the single layer model under different geomagnetic regions and ionospheric conditions, *J. Geod.*, *84*, 293–304, doi:10.1007/s00190-010-0367-5.

Chan, K. L., and O. G. Villard Jr. (1962), Observation of large-scale traveling ionospheric disturbances by spaced-path high-frequency instantaneous-frequency measurements, *J. Geophys. Res.*, *67*, 973–988, doi:10.1029/JZ067i003p00973.

Cherniak, I., I. Zakharenkova, and R. J. Redmon (2015), Dynamics of the high-latitude ionospheric irregularities during the 17 March 2015 St. Patrick's Day storm: Ground-based GPS measurements, *Space Weather*, *13*, 585–597, doi:10.1002/2015SW001237.

Davis, M. J. (1971), On polar substorms as the source of large-scale traveling ionospheric disturbances, *J. Geophys. Res.*, *76*, 4525–4533, doi:10.1029/JA076i019p04525.

Davis, M. J., and A. V. Da Rosa (1969), Traveling ionospheric disturbances originating in the auroral oval during polar substorms, *J. Geophys. Res.*, *74*, 5721–5735, doi:10.1029/JA074i024p05721.

Ding, F., W. Wan, Q. Li, R. Zhang, Q. Song, B. Ning, L. Liu, B. Zhao, and B. Xiong (2014), Comparative climatological study of large-scale traveling ionospheric disturbances over North America and China in 2011–2012, *J. Geophys. Res. Space Physics*, *119*, 519–529, doi:10.1002/2013JA019523.

Duly, T. M., N. P. Chapagain, and J. J. Makela (2013), Climatology of nighttime medium-scale traveling ionospheric disturbances (MSTIDs) in the central Pacific and South American sectors, *Ann. Geophys.*, *31*, 2229–2237, doi:10.5194/angeo-31-2229-2013.

Evans, J. V., J. M. Holt, and R. H. Wand (1983), A differential-Doppler study of traveling ionospheric disturbances from Millstone Hill, *Radio Sci.*, *18*, 435–451, doi:10.1029/RS018i003p00435.

Forbes, J. M., S. L. Bruinsma, Y. Miyoshi, and H. Fujiwara (2008), A solar terminator wave in thermosphere neutral densities measured by the CHAMP satellite, *Geophys. Res. Lett.*, *35*, L14802, doi:10.1029/2008GL034075.

Foster, J. C. (1993), Storm time plasma transport at middle and high latitudes, *J. Geophys. Res.*, *98*, 1675–1690, doi:10.1029/92JA02032.

Foster, J. C., and H. B. Vo (2002), Average characteristics and activity dependence of the subauroral polarization stream, *J. Geophys. Res.*, *107*(A12), 1475, doi:10.1029/2002JA009409.

Foster, J. C., and W. J. Burke (2002), SAPS: A new characterization for sub-auroral electric fields, *AGU*, *83*, 393–394.

Foster, J. C., W. Rideout, B. Sandel, W. T. Forrester, and F. J. Rich (2007), On the relationship of SAPS to storm-enhanced density, *J. Atmos. Terr. Phys.*, *69*, 303–313, doi:10.1016/j.jastp.2006.07.021.

Francis, S. H. (1974), A theory of medium-scale traveling ionospheric disturbances, *J. Geophys. Res.*, *79*, 5245–5260, doi:10.1029/JA079i034p05245.

Georges, T. M. (1968), HF Doppler studies of traveling ionospheric disturbances, *J. Atmos. Terr. Phys.*, *30*, 735–746, doi:10.1016/S0021-9169(68)80029-7.

Hayashi, H., N. Nishitani, T. Ogawa, Y. Otsuka, T. Tsugawa, K. Hosokawa, and A. Saito (2010), Large-scale traveling ionospheric disturbance observed by SuperDARN Hokkaido HF radar and GPS networks on 15 December 2006, *J. Geophys. Res.*, *115*, A06309, doi:10.1029/2009JA014297.

Hines, C. O. (1960), Internal atmospheric gravity waves at ionospheric heights, *Can. J. Phys.*, *38*, 1441–1481, doi:10.1139/p60-150.

Hocke, K., and K. Schlegel (1996), A review of atmospheric gravity waves and travelling ionospheric disturbances: 1982–1995, *Ann. Geophys.*, *14*, 917–940.

Hofmann-Wellenhof, B. (2001), *Global Positioning System: Theory and Practice*, Springer, New York.

Hofmann-Wellenhof, B., Lichtenegger, H., Wasle, E. (2008) *GNSS—Global Navigation Satellite Systems: GPS, GLONASS, Galileo, and More*, 518 pp., Springer, Vienna, doi:10.1007/978-3-211-73017-1.

Horvath, I., and S. Crozier (2007), Software developed for obtaining GPS-derived total electron content values, *Radio Sci.*, *42*, RS2002, doi:10.1029/2006RS003452.

Hunsucker, R. D. (1982), Atmospheric gravity waves generated in the high-latitude ionosphere: A review, *Rev. Geophys.*, *20*, 293–315, doi:10.1029/RG020i002p00293.

ICD-GLONASS (2008), *Global Navigation Satellite System GLONASS Interface Control Document, Version 5.1*, 73 pp., Russian Institute of Space Device Engineering, Moscow, Russia.

Jakowski, N., Y. Béniguel, G. De Franceschi, M. Hernández-Pajares, K. S. Jacobsen, I. Stanislawska, L. Tomasik, R. Warnant, and G. Wautelet (2012), Monitoring, tracking and forecasting ionospheric perturbations using GNSS techniques, *J. Space Weather Space Clim.*, *2*, A22, doi:10.1051/swsc/2012022.

Jeffrey, C. (2015), *An Introduction to GNSS: GPS, GLONASS, Galileo and Other Global Navigation Satellite Systems*, 91 pp., NovAtel Publisher, Calgary, Canada.

Kamide, Y., and K. Kusano (2015), No major solar flares but the largest geomagnetic storm in the present solar cycle, *Space Weather*, *13*, 365–367, doi:10.1002/2015SW001213.

Kirchengast, G. (1997), Characteristics of high-latitude TIDs from different causative mechanisms deduced by theoretical modeling, *J. Geophys. Res.*, *102*, 4597–4612, doi:10.1029/96JA03294.

Kirchengast, G., K. Hocke, and K. Schlegel (1996), The gravity wave-TID relationship: Insight via theoretical model-EISCAT data comparison, *J. Atmos. Terr. Phys.*, *58*, 233–243, doi:10.1016/0021-9169(95)00032-1.

Kotake, N., Y. Otsuka, T. Ogawa, T. Tsugawa, and A. Saito (2007), Statistical study of medium-scale traveling ionospheric disturbances observed with the GPS networks in Southern California, *Earth Planets Sp.*, *59*, 95–102, doi:10.1186/BF03352681.

Liu, J., W. Wang, A. Burns, X. Yue, S. Zhang, Y. Zhang, and C. Huang (2015), Profiles of ionospheric storm-enhanced density during the 17 March 2015 great storm, *J. Geophys. Res. Space Physics*, *121*, 727–744, doi:10.1002/2015JA021832.

Ma, G., and T. Maruyama (2003), Derivation of TEC and estimation of instrumental biases from GEONET in Japan, *Ann. Geophys.*, *21*, 2083–2093, doi:10.5194/angeo-21-2083-2003.

Maeda, S., and S. Handa (1980), Transmission of large-scale TIDs in the ionospheric F_2 region, *J. Atmos. Terr. Phys.*, *42*, 853–859, doi:10.1016/0021-9169(80)90089-6.

Melbourne, W. G. (1985), The case for ranging in GPS based geodetic systems, in *Proceedings of the 1st International Symposium on Precise Positioning with the Global Positioning System*, pp. 373–386, US Department of Commerce, Rockville, Md.

Mendillo, M., J. Baumgardner, D. Nottingham, J. Aarons, B. Reinisch, J. Scali, and M. Kelley (1997), Investigations of thermospheric-ionospheric dynamics with 6300 A images from the Arecibo Observatory, *J. Geophys. Res.*, *102*, 7331–7343, doi:10.1029/96JA02786.

Munro, G. H. (1948), Short period changes in the *F*-region of the ionosphere, *Nature*, *162*, 886–887, doi:10.1038/162886a0.

Natorf, L., K. Schlegel, and A. W. Wernik (1992), Gravity wave parameters derived from traveling ionospheric disturbances observations in the auroral zone, *Radio Sci.*, *27*, 829–840, doi:10.1029/92RS01649.

Nicolls, M. J., and C. J. Heinselman (2007), Three-dimensional measurements of traveling ionospheric disturbances with the Poker Flat Incoherent Scatter Radar, *Geophys. Res. Lett.*, *34*, L21104, doi:10.1029/2007GL031506.

Nicolls, M. J., M. C. Kelley, A. J. Coster, S. A. Gonzalez, and J. J. Makela (2004), Imaging the structure of a large-scale TID using ISR and TEC data, *Geophys. Res. Lett.*, *31*, L09812, doi:10.1029/2004GL019797.

Nishioka, M., A. Saito, and T. Tsugawa (2009), Super-medium-scale traveling ionospheric disturbance observed at midlatitude during the geomagnetic storm on 10 November 2004, *J. Geophys. Res.*, *114*, A07310, doi:10.1029/2008JA013581.

Onishi, T., T. Tsugawa, Y. Otsuka, J. J. Berthelier, and J. P. Lebreton (2009), First simultaneous observations of daytime MSTIDs over North America using GPS-TEC and DEMETER satellite data, *Geophys. Res. Lett.*, *36*, L11808, doi:10.1029/2009GL038156.

Otsuka, Y., K. Suzuki, S. Nakagawa, M. Nishioka, K. Shiokawa, and T. Tsugawa (2013), GPS observations of medium-scale traveling ionospheric disturbances over Europe, *Ann. Geophys.*, *31*, 163–172, doi:10.5194/angeo-31-163-2013.

Paul, A., A. Das, and A. DasGupta (2011), Characteristics of SBAS grid sizes around the northern crest of the equatorial ionization anomaly, *J. Atmos. Solar-Terrestrial Phys.*, *73*, 1715–1722, doi:10.1016/j.jastp.2011.03.008.

Perevalova, N. P., E. L. Afraimovich, S. V. Voeykov, and I. V. Zhivetiev (2008), Parameters of large-scale TEC disturbances during the strong magnetic storm on 29 October 2003, *J. Geophys. Res.*, *113*, A00A13, doi: 10.1029/2008JA013137.

Pradipta, R., C. E. Valladares, B. A. Carter, and P. H. Doherty (2016), Interhemispheric propagation and interactions of auroral traveling ionospheric disturbances near the equator, *J. Geophys. Res. Space Physics*, *121*, 2462–2474, doi:10.1002/2015JA022043.

Reinisch, B. W., and I. A. Galkin (2011), Global Ionospheric Radio Observatory (GIRO), *Earth Planets Space*, *63*, 377–381, doi:10.5047/eps.2011.03.001.

Reinisch, B. W., J. L. Scali, and D. M. Haines (1998), Ionospheric drift measurements with ionosondes, *Ann. Geofis.*, *41*(5–6), 695–702.

Russian IAC PNT (2016), (Information and Analysis Center for Positioning, Navigation and Timing). FTP server. [Available at ftp://ftp.glonass-iac.ru/MCC/ALMANAC/As accessed on 5 October.]

Saito, A., S. Fukao, and S. Miyazaki (1998), High resolution mapping of TEC perturbations with the GSI GPS network over Japan, *Geophys. Res. Lett.*, *25*, 3079–3082, doi:10.1029/98GL52361.

Saito, A., et al. (2001), Traveling ionospheric disturbances detected in the FRONT campaign, *Geophys. Res. Lett.*, *28*, 689–692, doi:10.1029/2000GL011884.

Shiokawa, K., Y. Otsuka, T. Ogawa, N. Balan, K. Igarashi, A. J. Ridley, D. J. Knipp, A. Saito, and K. Yumoto (2002), A large-scale traveling ionospheric disturbance during the magnetic storm of 15 September 1999, *J. Geophys. Res.*, *107*, 1088, doi:10.1029/2001JA000245.

Shiokawa, K., C. Ihara, Y. Otsuka, and T. Ogawa (2003), Statistical study of nighttime medium-scale traveling ionospheric disturbances using midlatitude airglow images, *J. Geophys. Res.*, *108*(A1), 1052, doi:10.1029/2002JA009491.

Shiokawa, K., Y. Otsuka, T. Tsugawa, T. Ogawa, A. Saito, K. Ohshima, M. Kubota, T. Maruyama, M. Yamamoto, and P. Wilkinson (2005), Geomagnetic conjugate observation of nighttime medium-scale and large-scale traveling ionospheric disturbances: FRONT3 campaign, *J. Geophys. Res.*, *110*, A05303, doi:10.1029/2004JA010845.

Song, Q., F. Ding, W. Wan, B. Ning, L. Liu, and B. Zhao (2013), Statistical study of large-scale traveling ionospheric disturbances generated by the solar terminator over China, *J. Geophys. Res. Space Physics*, *118*, 4583–4593, doi:10.1002/jgra.50423.

Sur, D., S. Ray, and A. Paul (2015), Role of neutral wind in the performance of artificial neural-network based TEC models at diverse longitudes in the low latitudes, *J. Geophys. Res. Space Physics*, *120*, 5009–5021, doi:10.1002/2015JA021023.

Tedd, B. L., and M. G. Morgan (1985), TID observations at spaced geographic locations, *J. Geophys. Res.*, *90*, 307–319, doi:10.1029/JA090iA12p12307.

Tsugawa, T., and A. Saito (2004), A statistical study of large-scale traveling ionospheric disturbances using the GPS network in Japan, *J. Geophys. Res.*, *109*, A06302, doi:10.1029/2003JA010302.

Tsugawa, T., A. Saito, Y. Otsuka, and M. Yamamoto (2003), Damping of large-scale traveling ionospheric disturbances detected with GPS networks during the geomagnetic storm, *J. Geophys. Res.*, *108*(A3), 1–14, doi:10.1029/2002JA009433.

Tsugawa, T., Y. Otsuka, A. J. Coster, and A. Saito (2007), Medium-scale traveling ionospheric disturbances detected with dense and wide TEC maps over North America, *Geophys. Res. Lett.*, *34*, L22101, doi:10.1029/2007GL031663.

Valladares, C. E., J. Villalobos, M. A. Hei, R. Sheehan, S. Basu, E. MacKenzie, P. H. Doherty, and V. H. Rios (2009), Simultaneous observation of traveling ionospheric disturbances in the Northern and Southern Hemispheres, *Ann. Geophys.*, *27*, 1501–1508, doi:10.5194/angeo-27-1501-2009.

van De Kamp, M., D. Pokhotelov, and K. Kauristie (2014), TID characterised using joint effort of incoherent scatter radar and GPS, *Ann. Geophys.*, *32*, 1511–1532, doi:10.5194/angeo-32-1511-2014.

Wanninger, L. (2012), Carrier-phase inter-frequency biases of GLONASS receivers, *J. Geod.*, *86*, 139–148, doi:10.1007/s00190-011-0502-y.

Wübbena, G. (1985), Software developments for geodetic positioning with GPS using TI 4100 code and carrier measurements, in *Proceedings of the 1st International Symposium on Precise Positioning with the Global Positioning System*, pp. 403–412, US Department of Commerce, Rockville, Md.

Zhang, S., et al. (2015), Thermospheric poleward wind surge at midlatitudes during great storm intervals, *Geophys. Res. Lett.*, *42*, 5132–5140, doi:10.1002/2015GL064836.